

To appear in the *Astrophysical Journal*

# Tracing the Milky Way Nuclear Wind with 21cm Atomic Hydrogen Emission

Felix J. Lockman<sup>1</sup>

*National Radio Astronomy Observatory, Green Bank, WV 24944*

`jlockman@nrao.edu`

N. M. McClure-Griffiths

*Research School of Astronomy & Astrophysics, The Australian National University,  
Canberra ACT 2611, Australia*

`naomi.mcclure-griffiths@anu.edu.au`

## ABSTRACT

There is evidence in 21cm H I emission for voids several kpc in size centered approximately on the Galactic center, both above and below the Galactic plane. These appear to map the boundaries of the Galactic nuclear wind. An analysis of H I at the tangent points, where the distance to the gas can be estimated with reasonable accuracy, shows a sharp transition at Galactic radii  $R \lesssim 2.4$  kpc from the extended neutral gas layer characteristic of much of the Galactic disk, to a thin Gaussian layer with FWHM  $\sim 125$  pc. An anti-correlation between H I and  $\gamma$ -ray emission at latitudes  $10^\circ \leq |b| \leq 20^\circ$  suggests that the boundary of the extended H I layer marks the walls of the Fermi Bubbles. With H I we are able to trace the edges of the voids from  $|z| > 2$  kpc down to  $z \approx 0$ , where they have a radius  $\sim 2$  kpc. The extended HI layer likely results from star formation in the disk, which is limited largely to  $R \gtrsim 3$  kpc, so the wind may be expanding into an area of relatively little H I. Because the H I kinematics can discriminate between gas in the Galactic center and foreground material, 21cm H I emission may be the best probe of the extent of the nuclear wind near the Galactic plane.

*Subject headings:* Galaxy: center — Galaxy: halo — ISM: jets and outflows  
ISM: kinematics and dynamics

---

<sup>1</sup>The National Radio Astronomy Observatory is a facility of the National Science Foundation operated under a cooperative agreement by Associated Universities, Inc.

## 1. Introduction

The nuclei of galaxies often launch fast moving winds from active bursts of star formation or accretion events onto a central supermassive black hole (see the review by Veilleux et al. 2005). The Milky Way appears to be no exception. Over the past three decades direct evidence for a nuclear wind has been mounting. Evidence has come from across the electromagnetic spectrum, including extended soft X-ray emission (Snowden et al. 1997; Sofue 2000; Bland-Hawthorn & Cohen 2003), diffuse microwave excess from WMAP (Finkbeiner 2004; Dobler et al. 2010) and polarized radio continuum (Carretti et al. 2013). The imaging of excess  $\gamma$ -ray emission extending to latitudes  $|b| \sim 55^\circ$  confirmed the existence and full extent of the Milky Way’s nuclear wind structures, now known as the Fermi Bubbles (Su et al. 2010; Ackermann et al. 2014). Furthermore, there is now direct detection of gas within the outflow, measured through absorption lines in ionized species towards background AGN (Keeney et al. 2006; Fox et al. 2015) and in atomic hydrogen emission (McClure-Griffiths et al. 2013). There is also indirect evidence: the H I layer at  $R \lesssim 3$  kpc is noticeably thin and lacks the vertical extensions characteristic of most of the disk (Lockman 1984) suggesting that it might have been excavated by a Galactic wind (e.g., Bregman 1980).

Much about the nuclear wind is unknown including its energy source, which may be an outburst from the central black hole, or the product of star formation, either episodic or continuous. Likewise, estimates for the age and timescale for evolution of the wind vary by more than an order of magnitude, from a few 10 Myr to a few hundred Myr (e.g., Bland-Hawthorn & Cohen 2003; Su et al. 2010; Lacki 2014; Sarkar et al. 2015; Crocker et al. 2015). The wind has internal structure and is not symmetric, and this manifests itself in the offset of various tracers from each other; there are also asymmetries observed that may indicate multiple energetic events or perturbations to the wind structure arising in environmental influences, either internal to the Milky Way or external (Crocker et al. 2015; Kataoka et al. 2015; Sarkar et al. 2015).

It is difficult to discern the shape of the Bubbles at low Galactic latitudes using tracers that do not carry kinematic information because of confusion with unrelated material and foreground structures such as Loop I. To determine the morphology of the Fermi Bubbles in  $\gamma$ -rays, e.g., foreground  $\gamma$ -ray emission must be estimated and removed. Here we use the velocity structure of the H I line together with a model of Galactic kinematics to separate emission originating near the Galactic center from that of the intervening medium. If the Fermi Bubbles are filled with hot gas, they should appear as voids in H I which can be used to map the morphology of the Bubbles at low latitudes.

Throughout this work we adopt the Sun-center distance and LSR rotational velocity  $R_0 = 8.5$  kpc, and  $|V_0| = 220$  km s $^{-1}$ , and, for consistency, scale previous work to these

values. Although the earlier results (Lockman 1984) were obtained using a simple model of circular rotation with some density-wave streaming, the subsequent characterization of the bar in the Milky Way (Blitz & Spergel 1991) allows us to use more accurate models for Galactic kinematics (e.g., Weiner & Sellwood 1999).

## 2. An H I Image of the Galactic Center

### 2.1. The H I data

We use 21cm H I data from the Parkes Galactic All-Sky Survey (GASS; McClure-Griffiths et al. 2009; Kalberla et al. 2010), the most recent version of which has improved spectral baselines (Kalberla & Haud 2015), for investigation of the nuclear wind. The GASS spectra were obtained using the Parkes radio telescope. The survey has an angular resolution of  $16'$ , a velocity channel spacing of  $0.8 \text{ km s}^{-1}$ , and an rms noise of 57 mK. The GASS data have uniform coverage over the area of this study, at  $|\ell| < 30^\circ$  and  $|b| < 30^\circ$  for  $\delta \lesssim 0^\circ$ .

### 2.2. Terminal Velocities and Tangent Points

On sight-lines interior to the solar circle at galactocentric distances  $R < R_0 \equiv 8.5 \text{ kpc}$ , the projection of Galactic rotational velocities  $V_\theta(R)$  onto the LSR is greatest at the tangent points where  $R_t = R_0 |\sin(\ell)|$ . These tangent points are at a distance from the Sun (at  $b \approx 0^\circ$ ) of  $d_t = R_0 \cos(\ell)$ , and here any radial or vertical motions,  $V_R$  or  $V_z$ , are projected across the line of sight and do not appear in  $V_{\text{LSR}}$ . Provided that azimuthal streaming motions are not too large, the maximum measured positive (negative) velocity of H I emission in the first (fourth) longitude quadrant,  $V_{\text{max}}(\ell)$ , can thus be equated to the terminal velocity from Galactic rotation,  $V_t$ , and the emission assigned to  $d_t$  and  $R_t$ . A discussion of potential uncertainties associated with this chain of reasoning is given in the Appendix.

There will always be some H I emission at  $|V_{\text{LSR}}| > |V_t|$  because of random motions in the interstellar gas, and this can be accounted for in determining  $V_{\text{max}}$ . Another factor that must be considered is the change in  $V_{\text{LSR}}$  with distance, which is a strong function of longitude and distance. This determines the spatial interval around  $d_t$  that contributes emission in a velocity range around  $V_t$ . The issues are well understood (e.g., Burton & Gordon 1978; Lockman 1984; Celnik et al. 1979; Malhotra 1995; McClure-Griffiths & Dickey 2007). For this investigation we use the Weiner & Sellwood (1999) model of gas kinematics in the inner Galaxy (hereafter WS), which includes the dynamical effects of a bar, adjusted to  $|V_0| = 220 \text{ km s}^{-1}$  and  $R_0 = 8.5 \text{ kpc}$ . At each longitude we evaluate the maximum value

of  $|V_{\text{LSR}}|$  appropriate to the inner Galaxy and set that equal to  $|V_t|$ .

Our general results do not depend on specific properties of the WS bar model; use of the models of Fux (1999) or Rodriguez-Fernandez & Combes (2008) would lead to qualitatively identical conclusions. The results are also robust to assumptions about the exact Galactic rotation curve, the existence of density-wave streaming motions, or Galactic constants.

### 3. Voids in H I Above and Below the Galactic Plane

Figure 1 shows the H I emission as a function of longitude and  $V_{\text{LSR}}$ , with values of  $V_{\text{max}}$  from the WS model as blue points. The central panel shows H I averaged over latitudes  $|b| < 2^\circ$ , while the upper and lower panels show the same curves on H I emission averaged over  $3^\circ < b < 5^\circ$  and  $-5^\circ < b < -3^\circ$ , respectively.

It is apparent that at  $b \approx 0^\circ$  (central panel) velocities around  $V_{\text{max}}$  contain H I emission at all longitudes, but only a few degrees above and below the plane there are large voids in  $(\ell - V)$  space spanning more than  $15^\circ \times 100 \text{ km s}^{-1}$ . Within these voids there is only occasional H I emission; it can be identified with non-circular motions arising from the Galactic bar or conditions in the inner nucleus (e.g., Oort 1977; Burton & Liszt 1978; Binney et al. 1991; Rodriguez-Fernandez & Combes 2008).

It is known that extra-planar gas in many spiral galaxies has a vertical lag in rotational velocity  $dV_\theta/dz \approx -10 \text{ km s}^{-1} \text{ kpc}^{-1}$  (Sancisi et al. 2001). The lag likely originates from the interaction between H I clouds and a more slowly rotating hot galactic corona (e.g., Fraternali & Binney 2008; Melioli et al. 2009; Marasco et al. 2015). In the Milky Way a measurement about 3 kpc above a superbubble gives a lag of  $-8 \text{ km s}^{-1} \text{ kpc}^{-1}$  while model fits to large-scale H I surveys find a value about twice as large,  $-15 \text{ km s}^{-1} \text{ kpc}^{-1}$  (Pidopryhora et al. 2007; Marasco & Fraternali 2011). A lag of this magnitude cannot account for the voids in Fig. 1, which appear abruptly at  $\ell \sim \pm 15^\circ$  from the Galactic center and are fully formed by  $|z| \approx 0.25 \text{ kpc}$ . To create the voids from a rotational lag, Galactic rotation would have to be reduced by more than  $100 \text{ km s}^{-1}$  at  $|z| = 0.25 \text{ kpc}$ , and would have to fall to near zero at  $|z| \approx 0.5 \text{ kpc}$ . In actuality, ample gas with a very small lag, if any, is found at  $z = 0.5 \text{ kpc}$  for  $R \gtrsim 3 \text{ kpc}$  (e.g., Lockman 2002; Ford et al. 2010).

The voids in longitude and velocity thus imply that there are large volumes of space with little neutral Hydrogen in the inner Galaxy. To quantify the extent of the voids at all locations in the inner Galaxy would require a detailed model of the Galaxy’s kinematics and the result would not be unique, but the basic parameters of the voids can be determined from an analysis along the tangent points, as identified by  $V_{\text{max}}$ , where the distance can be

determined with reasonable accuracy.

Setting  $V_t = V_{max}$  derived from the WS model, at each longitude and latitude we have calculated the tangent-point H I emission over a velocity interval around  $V_t$ . In the first quadrant of longitude this can be written

$$N_H(\ell, b) = 1.823 \times 10^{18} \int_{V_t - \Delta v_1}^{V_t + \Delta v_2} \tau(v) T_b(v) dv \text{ cm}^{-2}. \quad (1)$$

This equation was also applied to the fourth longitude quadrant with a suitable change of sign in the velocities. The velocity interval  $\Delta v_1$  is chosen from the WS model as described in the Appendix to encompass a line-of-sight distance of approximately 1 kpc around the tangent point. It takes a value of 3 km s<sup>-1</sup> for longitudes  $|\ell| > 20^\circ$ , increases slowly between  $|\ell| = 20^\circ$  and  $|\ell| = 8^\circ$  to 10 km s<sup>-1</sup>, increasing rapidly thereafter to 50 km s<sup>-1</sup> at  $|\ell| = 5^\circ$ . Because of the substantial non-circular motions that are associated with the Galactic nucleus near  $\ell = 0^\circ$ , we arbitrarily limit  $\Delta v_1$  to 50 km s<sup>-1</sup> within  $5^\circ$  of the Galactic center, with consequences discussed in the Appendix. The innermost part of the Galactic disk is associated with large non-circular motions in all species (e.g., Burton & Liszt 1993), so our results lose accuracy at  $R \lesssim 1$  kpc. The upper velocity limit,  $\Delta v_2 = 30$  km s<sup>-1</sup>, is held constant with longitude and was chosen to capture most of the H I emission in the wings of the profiles (Kulkarni & Fich 1985; McClure-Griffiths & Dickey 2007). The velocity limits are shown as grey lines around  $V_t$  in the central panel of Figure 1. We estimate the optical depth per channel from the brightness temperature,  $T_b$ , of the emission, where  $\tau(v) = -\ln(1 - T_b(v)/T_s)$ , with an assumed gas spin temperature  $T_s = 150$  K (e.g., Dickey & Lockman 1990). Figure 2 shows the optical depth corrected column density as a function of longitude and latitude.

Figure 2 shows that there are two large cavities in Galactic H I at  $|b| \gtrsim 2^\circ$  over longitudes  $-15^\circ \lesssim \ell \lesssim 17^\circ$ . Within these cavities there is almost no detectable H I emission with the exception of a few small, isolated clouds that have typical column densities of  $N_{\text{HI}} < 7 \times 10^{18} \text{ cm}^{-2}$ , likely related to the population of H I clouds discovered to be entrained in the nuclear wind (McClure-Griffiths et al. 2013). For the adopted Sun-center distance  $R_0 = 8.5$  kpc, the region devoid of H I extends from  $R \approx 2.1$  kpc on the negative longitude (Southern) side of the Galactic center to  $R \approx 2.4$  kpc on the positive longitude (Northern) side of the Galactic center.

The general features of this Figure do not depend on the details of the adopted  $V_t(\ell)$  function or the precise values of  $\Delta v_1$  and  $\Delta v_2$ . As is obvious from Fig. 1, the large voids above and below the plane will map into spatial voids centered approximately on the Galactic center.

### 3.1. Gas Distribution and Mass

Figures 1 and 2 confirm the absence of gas in an extended H I layer within 3 kpc of the Galactic center. To demonstrate this more quantitatively, we plot the distribution of mean column density,  $\langle N_{\text{HI}} \rangle$ , versus distance from the Galactic plane,  $z$ , for several ranges of galactocentric radius in Figure 3. The column density is from Figure 2 in intervals of  $R$  averaged over both positive and negative Galactic longitudes. The distribution within  $R < 2$  kpc is well described by a single Gaussian of FWHM  $\sim 125$  pc, whereas at  $R > 2.75$  kpc the disk and lower halo require the well-known two Gaussian components with FWHM  $\sim 150$  pc and  $\sim 400$  pc, plus an extended exponential tail of  $\sim 500$  pc (Lockman 1984; Lockman et al. 1986; Savage & Massa 1987; Dickey & Lockman 1990; Savage & Wakker 2009). In the transition region around  $R \sim 2$ – $2.5$  kpc the distribution is described by two Gaussians of width 100 and 300 pc, without an additional exponential component. These functions are drawn in Fig. 3 as dashed lines.

To convert from a column density measured in the plane of the sky to either a number density of hydrogen or a surface density it is necessary to know the distance,  $\Delta d$ , that contributes to the emission at the terminal velocity. As described above, the velocity interval for the column density calculation was chosen to give a depth  $\Delta d \approx 1$  kpc at all longitudes. We use this to estimate the average number density of H I,  $n(z)$ , in bins of radius. The surface density,  $\Sigma_{\text{HI}}$ , is then  $n(z)$  integrated through the  $z$  direction for each radius bin. These values are given in Table 1. Because of the uncertainties in converting from a velocity interval to  $\Delta d$ , the errors on the surface density may be as large as a factor of two, but even so, it is clear that there is a significant decrease in H I surface density towards the center of the Milky Way, nearly an order of magnitude decrease between  $R > 3$  kpc and  $R < 2$  kpc.

## 4. Comparison with the Fermi Bubbles

Overlaid on the H I image of Fig. 2 is the Su et al. (2010) template for the Fermi Bubble edges (red circles) and their so-called “northern arc” (cyan circles), which is an excess of  $\gamma$ -ray emission surrounding the positive longitude edge of the Bubble. For  $\ell < 0^\circ$  and  $|b| > 10^\circ$  the H I void edges match the Su et al. (2010) Fermi Bubble templates reasonably well. In contrast, at  $\ell > 0^\circ$  the H I fails to match the Bubble template at any latitude; the Fermi Bubble template lies well within the H I void. However, the H I emission at positive longitudes and  $b > 0^\circ$  does match the inner edge of the so-called “Northern Arc”. Because of uncertainties in modelling and subtracting the foreground, the Su et al. (2010) template at  $|b| < 10^\circ$  is necessarily uncertain, and more recent work on the morphology of the Fermi Bubbles by Ackermann et al. (2014) does not attempt to quantify the Bubble emission within

10° of the Galactic plane.

If the Fermi Bubbles are filled with a hot plasma the absence of H I within the Bubble structures is not surprising. Figure 4 is a comparison between the H I emission averaged in latitude bins and the Fermi  $\gamma$ -ray emission (Ackermann et al. 2014) in the same bins. The H I data are the same as shown in Fig. 2. Systematic errors in the 21cm spectral baselines produce systematic errors in the derived  $\langle N_{\text{HI}} \rangle$  at the level of  $10^{18} \text{ cm}^{-2}$ . This corresponds to a baseline offset of  $< 1\sigma$  of the channel noise over  $20 \text{ km s}^{-1}$ . There is clearly an anti-correlation between the  $\gamma$ -ray emission and the H I emission: the H I emission is absent throughout the longitude range that shows GeV emission but appears where the Fermi  $\gamma$ -ray emission decreases.

Uncertainties in the foreground subtraction required for extracting  $\gamma$ -ray emission make estimates of the shape of the Fermi Bubbles at  $|b| < 10^\circ$  from high energy observations prone to significant errors. The H I kinematics, on the other hand, allows a clear separation of the emission originating at small Galactic radii from emission which is unrelated. Moreover, the  $\gamma$ -ray emission that traces the Fermi Bubbles does not necessarily give a complete picture of the location and extent of the nuclear wind volume, as shown in recent models for the Bubbles (Crocker et al. 2015; Sarkar et al. 2015). At low latitudes the H I distribution should be a better tracer of the shape of the nuclear wind region than the  $\gamma$ -rays and the Fermi Bubbles.

## 5. Comparison with Star Forming Regions

The extended H I layer so visible in Fig. 2 at  $|\ell| \gtrsim 15^\circ$  almost certainly results from large-scale star formation processes, as verified by correlations observed both in the Milky Way and a variety of other galaxies (Ford et al. 2010; Heald 2015), though we lack a detailed understanding of the process. As the rate of star formation varies significantly across the Galaxy, it is worthwhile to consider whether the voids we describe might result in some part from the absence of an extended H I layer owing to a reduced star formation rate in the inner Galaxy.

We take as the measure of recent star formation the location of H II regions in the inner Galaxy from the WISE catalog (Anderson et al. 2014). In Fig. 2 the yellow dots show the longitude and latitude of H II regions selected under the same kinematic criteria used to select the H I. The H II regions are prevalent at the tangent points, and wherever there are H II regions there is the extended H I layer. The extended H I layer, however, does not cut off at the edge of the star forming regions but extends to lower  $|\ell|$ , and thus closer to the

Galactic center.

Fig. 5 shows the surface density of H II regions over  $6.2^\circ \leq |\ell| \leq 80^\circ$  against distance from the Galactic center, derived assuming a flat rotation curve with  $V_\theta = 220 \text{ km s}^{-1}$ . The vertical line shows the approximate boundary of the extended H I layer. Although there is a general correlation between the absence of H II regions at small values of  $R$  and the absence of an extended H I layer, it again appears that the H I is found much closer to the Galactic center than the H II regions. The H I voids do not seem to be simply a consequence of the low star formation activity at  $R \lesssim 2.4 \text{ kpc}$ . Moreover, the boundary of the H I void is relatively sharp (Fig. 4) whereas the H II region surface density decreases gradually at  $R < 4 \text{ kpc}$ . Still, the absence of significant star formation at  $0.2 \lesssim R \lesssim 3.5 \text{ kpc}$  suggests that the nuclear wind may be expanding through a medium that initially had less of an extended H I component than exists throughout the main Galactic disk.

## 6. Discussion and Summary

The absence of extra-planar H I within  $R \sim 2.6 \text{ kpc}$  of the Galactic center was first noted by Lockman (1984). Using more modern data, we find that at  $R \lesssim 2.1 \text{ kpc}$  on the Southern side of the Galactic center and  $R \lesssim 2.4 \text{ kpc}$  on the Northern side the H I layer is well described by a single Gaussian component of FWHM  $\sim 125 \text{ pc}$ . Beyond  $R > 3.5 \text{ kpc}$  the distribution returns to the well-known double Gaussian (FWHMs  $\sim 150 \text{ pc}$  and  $400 \text{ pc}$ ) plus an exponential tail. At intermediate radii the distribution is better described by the double Gaussian alone. The total surface density of H I is nearly an order of magnitude smaller at  $R < 2 \text{ kpc}$  than it is at  $R \geq 3.5 \text{ kpc}$ . A decrease in  $\Sigma_{HI}$  is often observed in the inner regions of spiral galaxies including the Milky Way (e.g. Roberts 1967; Wong & Blitz 2002; Burton & Gordon 1978), but here we have the favorable viewing angle that allows us to show that for the Milky Way about 20% of the missing H I can be attributed to the absence of the vertically extended H I layer, which terminates at a relatively sharp boundary (Fig. 4).

These results are based on an analysis of H I kinematics, and thus rely on the assumption that the WS model (or any model that matches the terminal velocities in the plane, (e.g., Fux 1999; Rodriguez-Fernandez & Combes 2008)) applies not only in the plane but vertically for several hundred parsecs. The H I data alone cannot rule out the existence of an extreme vertical kinematic anomaly such as a rotational lag of  $-400 \text{ km s}^{-1} \text{ kpc}^{-1}$  in the inner Galaxy. However, the general symmetry of the kinematic voids, their rapid onset  $\sim 15^\circ$  from the center, their correlation with the edges of the Fermi Bubbles, and the detection of H I and ionized gas apparently entrained in the nuclear wind (McClure-Griffiths et al. 2013; Fox



et al. 2015), all suggest that the simpler picture of a spatial void in extra-planar H I around the Galactic center is more likely.

A high energy, hot, nuclear wind should excavate diffuse H I from its vicinity and thus H I emission should be anti-correlated with the hot  $\gamma$ -ray emitting plasma (Veilleux et al. 2005). At Galactic latitudes  $|b| > 10^\circ$ , where the excess  $\gamma$ -ray emission of the Fermi Bubbles has been carefully extracted, we have found that the H I is very well anti-correlated with the  $\gamma$ -ray emission. Because the kinematics of H I allows spatial separation of Galactic center emission from unrelated material, it should provide the best tracer of the extent of the Fermi Bubbles, and hence the nuclear wind, within a few degrees of the Galactic plane, at the latitudes where foreground modelling makes estimating the high-energy emission particularly difficult.

Because the H I voids occur in the inner Galaxy where, outside of the innermost few hundred pc, the rate of star formation is low, the nuclear wind likely expanded through an ISM considerably less dense and extensive than is found further from the Galactic center.

The images we have provided give an indication of the somewhat surprising morphology of the nuclear wind, which, if we interpret the dimensions of the H I voids as deriving entirely from the wind, appear to extend to  $R \sim 2.4$  kpc at  $z \approx 0$ . Although the implied opening angle close to the plane may seem large, a recent hydrodynamic model of the Fermi Bubbles shows them extending to almost  $R \sim 2$  kpc at  $z \sim 1$  kpc (Sarkar et al. 2015). Whatever the source of the Fermi Bubbles, it has apparently left its mark on the large-scale distribution of H I in the inner Galaxy.

The Parkes Radio Telescope is part of the Australia Telescope which is funded by the Commonwealth of Australia for operation as a National Facility managed by CSIRO. We are grateful to D. Malayshev and A. Franckowiak for providing the Fermi GeV data in electronic form. We thank R. Benjamin, R. Crocker, C. Federrath, and H.A. Ford for valuable conversations while preparing this work.

*Facility:* Parkes

### A. $V_{max}$ , the Terminal Velocity, and the Tangent Point

Using a right-handed cylindrical coordinate system with the Sun at  $x = -R_0$ , the velocity of an object with respect to the LSR is

$$V_{LSR} = \left[ R_0 \sin \ell \left( \frac{V_0}{R_0} - \frac{V_\theta}{R} \right) + V_R \cos(\ell + \theta) \right] \cos b + V_z \sin b, \quad (\text{A1})$$

where  $R_0$  is the Sun-center distance, taken to be 8.5 kpc, and  $V_0$  the circular velocity of the LSR, taken to be  $-220 \text{ km s}^{-1}$  in this coordinate system. The azimuthal coordinate  $\theta$  runs opposite to Galactic rotation and thus  $\theta \approx \ell$  for an object at a great distance. Velocity components are  $V_R$ ,  $V_\theta$ , and  $V_z$ . At a tangent point the distance from the Sun is  $d_t = R_0 \cos(\ell)$ . Here also  $R_t = R_0 |\sin \ell|$ , and  $\theta - \ell = 90^\circ$ , so close to the Galactic plane where  $\cos b \approx 1.0$  and  $\sin b \approx 0$ , eq. A1 reduces to

$$V_{LSR} = [-V_\theta R_0 / R_t + V_0] \sin(\ell) \equiv V_t. \quad (\text{A2})$$

As  $R_t$  is the minimum distance from the Galactic center at all longitudes  $|\ell| < 90^\circ$ , unless  $V_\theta$  has a large variation over a fairly small distance,  $V_{LSR}$  will have its largest value at  $R_t$ , the tangent point: a positive velocity in the first quadrant of longitude, and a negative velocity in the fourth. It is therefore straightforward to identify emission associated with a particular tangent point and thus at a given distance.

In the Milky Way, however, streaming motions caused by density waves or the bar may produce conditions where the maximum velocity does not occur at the tangent point, but at another location, effecting the apparent rotation curve (e.g., Burton & Liszt 1993). This issue was considered recently by Chemin et al. (2015) who use the simulation of Renaud et al. (2013) to conclude that although streaming may produce errors in the derived rotation curve, for  $R \leq 6 \text{ kpc}$  the difference between the location of emission at  $V_{max}$  and the tangent point is only a few percent. As we are interested in a more general situation of associating a particular volume of space with the terminal velocity we elaborate on this issue for the bar model of Weiner & Sellwood (1999) (WS) used in our analysis.

We generated a set of test particles with a uniform surface density at  $R < R_0$  that follow the WS kinematics and have a random velocity component  $\sigma_{cc}$  as well. We calculate the particles  $\ell, b, z$ , and  $V_{LSR}$ , then analyze their properties in a manner identical to the way the H I data were analyzed. This allows us to determine how well our selection of tangent point gas represents the actual situation at that location.

Figure 6 shows the results of one of the simulations for a velocity dispersion  $\sigma_{cc} = 7 \text{ km s}^{-1}$  in  $R$ ,  $\theta$ , and  $z$ . Particles located within  $\pm 0.6 \text{ kpc}$  of the tangent points are colored red. Virtually all of the red points are located along the velocity limits of the simulation showing that, except for quite low longitudes, the tangent point sample occurs near  $V_{max}$ . Analyzing the simulation, we find that the location of  $V_{max}$  differs from the tangent point by usually  $\sim 5\%$  though at a few positions near  $\ell \sim 20^\circ$  the error can be as high as 20%. This

result is in general agreement with Chemin et al. (2015). Errors in the kinematic distance to individual objects located some distance from the tangent point can, however, be large, as illustrated by the HII region W31 (Sanna et al. 2014).

An equally important consideration for our work is the relationship between a velocity interval around  $V_{max}$  and the associated distance along the line of sight over which these velocities arise, parameterized by the quantity  $\Delta v_1$  in eq. 1. The importance of this in analyzing Galactic H I was emphasized by Burton (1972). While knowledge of  $\Delta v_1$  is needed to convert column densities to volume densities, for this investigation it is more important that we do not artificially produce structures (or remove them) by grossly changing the sample volume with longitude or  $R$ . Evaluating the WS model over the longitude range of interest, a 1 kpc distance corresponds to values for  $\Delta v_1$  that increase approximately linearly from 3 to 10 km s<sup>-1</sup> between  $\ell = 20^\circ$  and  $\ell = 8^\circ$ , and between 10 and 50 km s<sup>-1</sup> from  $\ell = 8^\circ$  to  $\ell = 5^\circ$ . For  $\ell \geq 20^\circ$  we use a constant value of  $\Delta v_1 = 3$  km s<sup>-1</sup> which increases the distance along the line of sight over which we average emission by a factor  $\approx 1.5$ . At  $\ell \leq 5^\circ$  a constant value  $\Delta v_1 = 50$  km s<sup>-1</sup> is adopted.

Figure 7 shows a face-on view of the results of the simulation, where points mark locations of clouds that would be included in the tangent-point analysis according to the selection criteria used for the H I. This is our estimate of the area of the Galaxy that contributes to Fig. 2. The choice of a constant  $\Delta v_1 = 50$  km s<sup>-1</sup> for  $\ell \leq 5^\circ$  limits the accuracy of this simulation at  $R \leq 0.75$ , but in any case our results are incomplete so close to the nucleus where strong non-circular motions make kinematic analysis difficult (e.g., Burton & Liszt 1978; Binney et al. 1991; Rodriguez-Fernandez & Combes 2008). The feature in the distribution around  $10^\circ \lesssim \ell \lesssim 20^\circ$  marks the area where streaming along the bar causes particles to have a significantly reduced  $V_{LSR}$  and thus not appear at  $V_t$ . No similar region exists in the South. There are no sharp discontinuities in the spatial coverage of our analysis that could artificially remove a real extended H I layer. As is evident in Figure 1, the absence of H I above and below the Galactic plane is a large-scale phenomenon in the inner Galaxy.

## REFERENCES

- Ackermann, M., Albert, A., Atwood, W. B., et al. 2014, *ApJ*, 793, 64
- Anderson, L. D., Bania, T. M., Balser, D. S., et al. 2014, *ApJS*, 212, 1
- Binney, J., Gerhard, O. E., Stark, A. A., Bally, J., & Uchida, K. I. 1991, *MNRAS*, 252, 210
- Bland-Hawthorn, J., & Cohen, M. 2003, *ApJ*, 582, 246

- Boothroyd, A. I., Blagrove, K., Lockman, F. J., et al. 2011, *A&A*, 536, A81
- Blitz, L., & Spergel, D. N. 1991, *ApJ*, 379, 631
- Bregman, J. N. 1980, *ApJ*, 236, 577
- Burton, W. B. 1972, *A&A*, 19, 51
- Burton, W. B., & Liszt, H. S. 1978, *ApJ*, 225, 815
- Burton, W. B., & Liszt, H. S. 1993, *A&A*, 274, 765
- Burton, W. B., & Gordon, M. A. 1978, *A&A*, 63, 7
- Carretti, E., Crocker, R. M., Staveley-Smith, L., et al. 2013, *Nature*, 493, 66
- Celnik, W., Rohlfs, K., & Braunsfurth, E. 1979, *A&A*, 76, 24
- Chemin, L., Renaud, F., & Soubiran, C. 2015, *A&A*, 578, A14
- Crocker, R. M., Bicknell, G. V., Taylor, A. M., & Carretti, E. 2015, *ApJ*, 808, 107
- Dickey, J. M., & Lockman, F. J. 1990, *ARA&A*, 28, 215
- Dobler, G., Finkbeiner, D. P., Cholis, I., Slatyer, T., & Weiner, N. 2010, *ApJ*, 717, 825
- Finkbeiner, D. P. 2004, *ApJ*, 614, 186
- Ford, H. A., Lockman, F. J., & McClure-Griffiths, N. M. 2010, *ApJ*, 722, 367
- Fox, A. J., Bordoloi, R., Savage, B. D., et al. 2015, *ApJ*, 799, L7
- Fraternali, F., & Binney, J. J. 2008, *MNRAS*, 386, 935
- Fux, R. 1999, *A&A*, 345, 787
- Heald, G. 2015, *IAU Symposium*, 309, 69
- Kalberla, P. M. W., McClure-Griffiths, N. M., Pisano, D. J., et al. 2010, *A&A*, 521, 17
- Kalberla, P. M. W., & Haud, U. 2015, *A&A*, 578, A78
- Kataoka, J., Tahara, M., Totani, T., et al. 2015, *ApJ*, 807, 77
- Keeney, B. A., Danforth, C. W., Stocke, J. T., et al. 2006, *ApJ*, 646, 951
- Kulkarni, S. R., & Fich, M. 1985, *ApJ*, 289, 792

- Lacki, B. C. 2014, MNRAS, 444, L39
- Lockman, F. J. 1984, ApJ, 283, 90
- Lockman, F. J. 2002, ApJ, 580, L47
- Lockman, F. J., Hobbs, L. M., & Shull, J. M. 1986, ApJ, 301, 380
- Malhotra, S. 1995, ApJ, 448, 138
- Marasco, A., & Fraternali, F. 2011, A&A, 525, A134
- Marasco, A., Debattista, V. P., Fraternali, F., et al. 2015, MNRAS, 451, 4223
- Melioli, C., Brighenti, F., D’Ercole, A., & de Gouveia Dal Pino, E. M. 2009, MNRAS, 399, 1089
- McClure-Griffiths, N. M., & Dickey, J. M. 2007, ApJ, 671, 427
- McClure-Griffiths, N. M., Green, J. A., Hill, A. S., et al. 2013, ApJ, 770, L4
- McClure-Griffiths, N. M., Pisano, D. J., Calabretta, M. R., et al. 2009, ApJS, 181, 398
- Oort, J. H. 1977, ARA&A, 15, 295
- Pidopryhora, Y., Lockman, F. J., & Shields, J. C. 2007, ApJ, 656, 928
- Roberts, M. S. 1967, Radio Astronomy and the Galactic System, 31, 189
- Rodriguez-Fernandez, N. J., & Combes, F. 2008, A&A, 489, 115
- Sancisi, R., Fraternali, F., Oosterloo, T., & van Moorsel, G. 2001, Galaxy Disks and Disk Galaxies, 230, 111
- Sanna, A., Reid, M. J., Menten, K. M., et al. 2014, ApJ, 781, 108
- Sarkar, K. C., Nath, B. B., & Sharma, P. 2015, MNRAS, 453, 3827
- Savage, B. D., & Massa, D. 1987, ApJ, 314, 380
- Savage, B. D., & Wakker, B. P. 2009, ApJ, 702, 1472
- Snowden, S. L., Egger, R. J., Freyberg, M. J., et al. 1997, ApJ, 485, 125
- Sofue, Y. 2000, ApJ, 540, 224
- Su, M., Slatyer, T. R., & Finkbeiner, D. P. 2010, ApJ, 724, 1044

Veilleux, S., Cecil, G., & Bland-Hawthorn, J. 2005, *ARA&A*, 43, 769

Weiner, B. J., & Sellwood, J. A. 1999, *ApJ*, 524, 112

Wong, T., & Blitz, L. 2002, *ApJ*, 569, 157

Table 1. Annular averages of H I surface density

Radius range (kpc)	$\Sigma_{HI}$ ( $M_{\odot} \text{ pc}^{-2}$ )
$1.50 < R < 1.75$	0.4
$2.00 < R < 2.25$	0.6
$2.50 < R < 2.75$	1.6
$3.00 < R < 3.25$	3.0
$3.50 < R < 3.75$	3.4

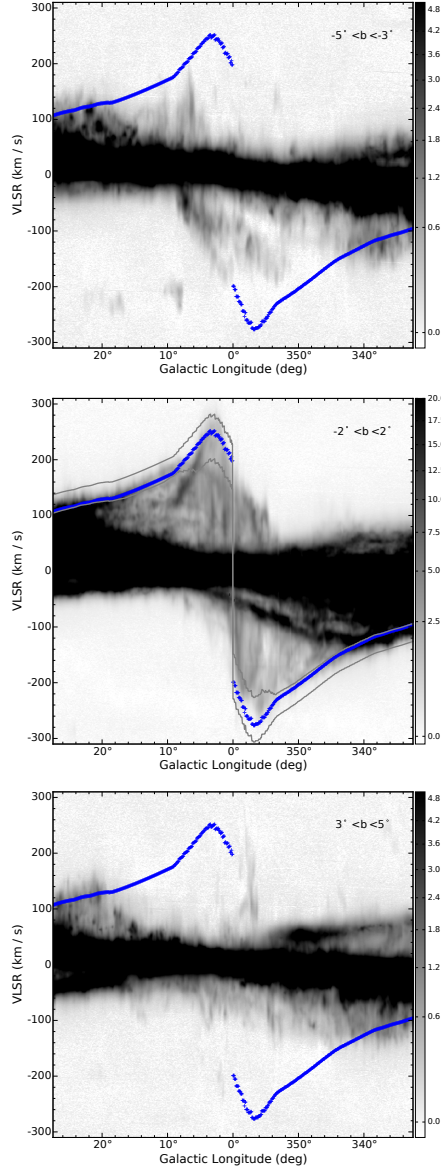


Fig. 1.— Longitude-velocity images of the averaged H I brightness temperature in the ranges  $3^\circ < b < 5^\circ$  (top),  $|b| < 2^\circ$  (middle), and  $-5^\circ < b < -3^\circ$  (bottom), overlaid with the terminal velocity values from the WS model (blue crosses) used to identify tangent point velocities. The H I is displayed with a square root transfer function in Kelvin, as shown in the wedges to the right. The grey lines around  $V_t$  in the central panel show the velocity limits used to integrate the emission included in Figure 2, and apply at all latitudes. At  $b \approx 0$  these velocity intervals encompass H I emission at all longitudes. However, there is little H I emission above and below the plane around  $V_t$  in the inner  $\pm 15^\circ$  of longitude. The absence of emission over a considerable range in  $V_{\text{LSR}}$  indicates that the voids are quite large. At the tangent points the average distance from the Galactic plane in the upper and lower panels varies from 0.4 kpc to 0.5 kpc.



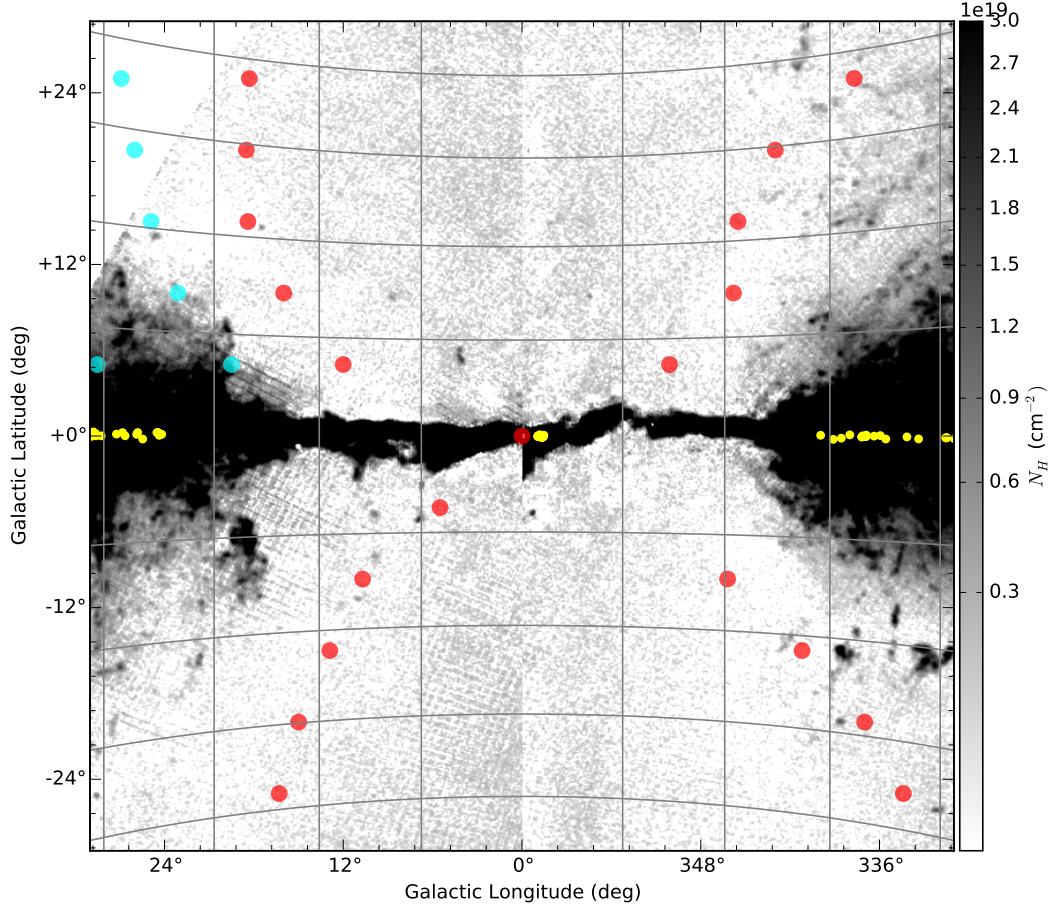


Fig. 2.— H I column density along the Galactic tangent points showing the absence of a vertically extended H I layer in the region around the Galactic center. The grid marks 1 kpc intervals in distance from the Galactic center and distance from the plane. The red dots show the outline of the Fermi Bubble template and the cyan dots show the outline of the “Northern Arc”, both as determined by Su et al. (2010). The greyscale is displayed in the wedge at the right with a square root transfer function. H I column densities in the range  $|l| < 5^\circ$  ( $R \leq 0.75$  kpc) are not reliable because of large non-circular motions associated with the Galactic center. The yellow dots mark the locations of tangent-point H II regions from the WISE catalog (Anderson et al. 2014) selected using the same kinematic filter used for the H I (eq. 1).

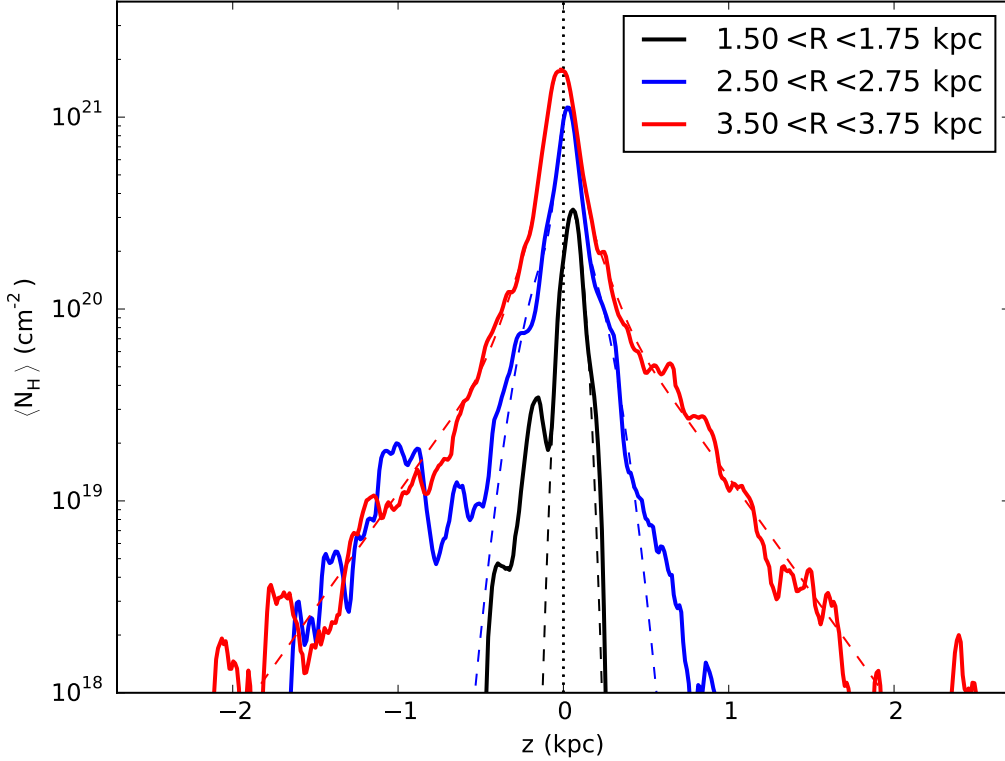


Fig. 3.— Average H I column density vs. distance from the Galactic plane in three bins of galactocentric radius,  $R$ , showing the absence of the extended H I layer towards the Galactic center. For  $R < 1.75$  kpc (black line) the H I distribution is described by a single Gaussian component of FWHM  $\sim 125$  pc. At  $R > 3.5$  kpc (red line), H I distribution is described by the well-known two Gaussian components (FWHM  $\sim 150$  pc and  $\sim 400$  pc) plus an extended exponential. At the intermediate radii (blue line) the distribution is reasonably well-described by two Gaussian components, but without the exponential. These curves include data from both Northern and Southern longitudes. Dashed lines show the values of the model fits.

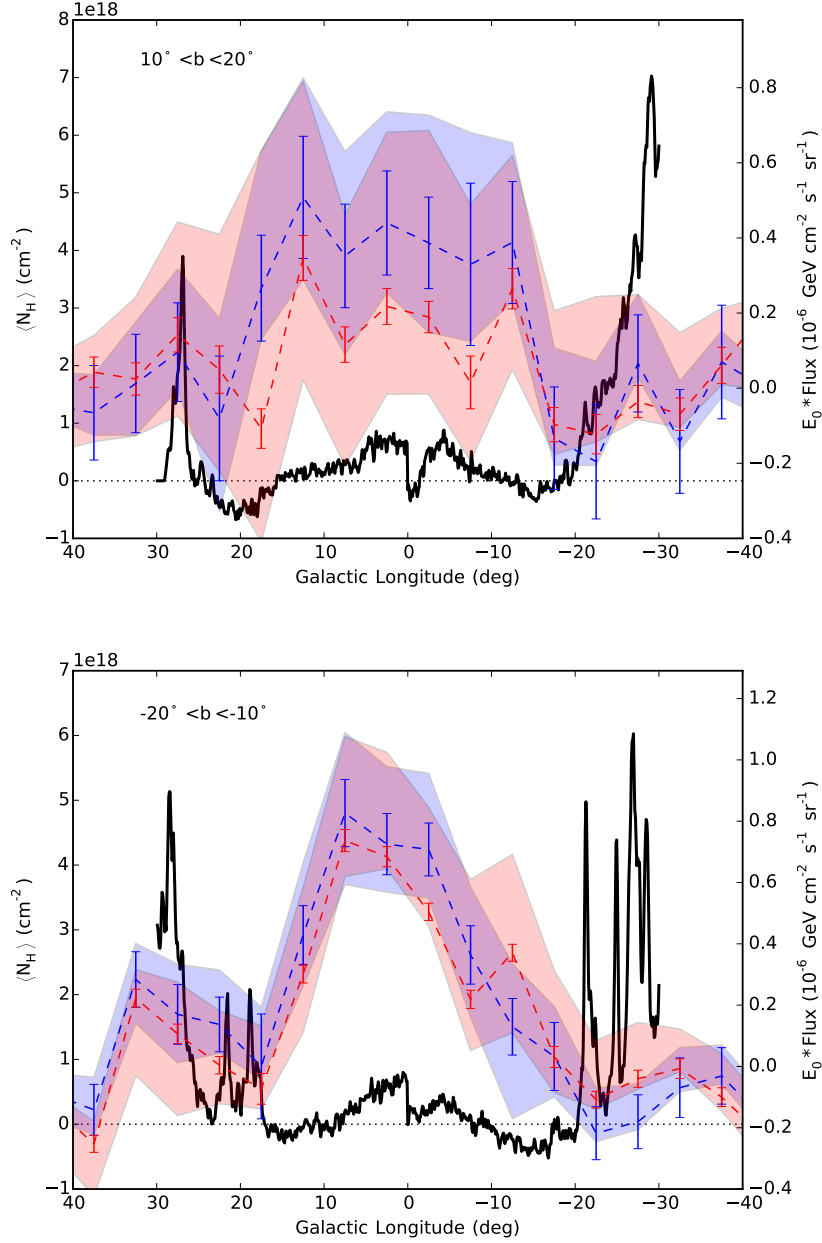


Fig. 4.— Comparison of the mean H I emission with Fermi LAT  $\gamma$ -ray emission at energies  $3 < E < 10 \text{ GeV}$  (red) and  $E > 10 \text{ GeV}$  (blue) reproduced from Ackermann et al. (2014) in two latitude bins  $10^\circ < b < 20^\circ$  (top) and  $-20^\circ < b < -10^\circ$  (bottom). The Fermi data are the Fermi Bubble residuals after subtraction of the GALPROP model and the shaded regions correspond to different foreground models as described in Ackermann et al. (2014). H I column densities in the range  $|l| < 5^\circ$  are not reliable because of unmodelled kinematic effects associated with the Galactic center. The anti-correlation between H I and  $\gamma$ -ray emission suggests that the H I voids trace the Fermi Bubbles. The figures average over distances from the plane of  $1.5 \lesssim |z| \lesssim 3.0 \text{ kpc}$ . Systematic baseline errors in the H I spectra below the  $1\sigma$  channel noise produce offsets in  $\langle N_{HI} \rangle$  with a magnitude  $\sim 10^{18} \text{ cm}^{-2}$ .

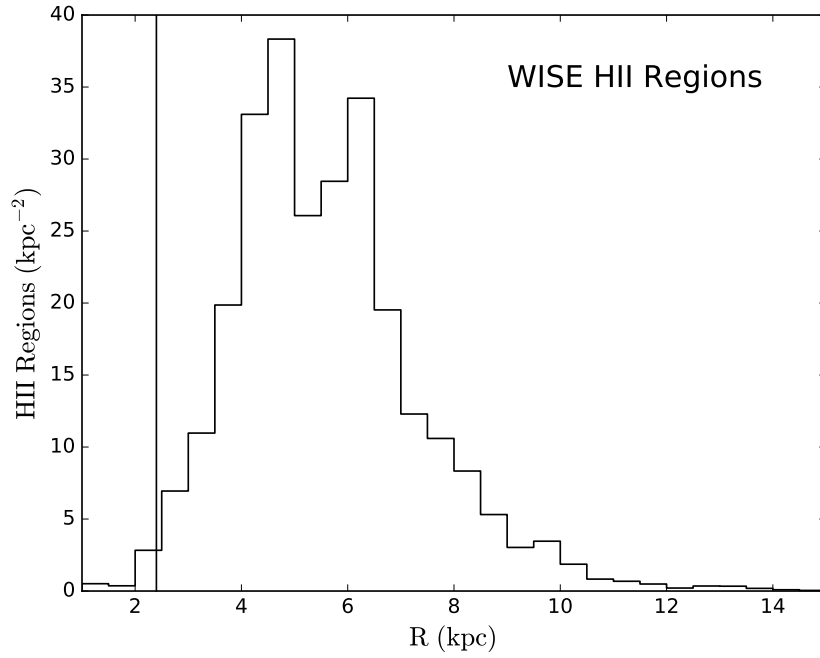


Fig. 5.— Surface density of H II regions from the WISE survey (Anderson et al. 2014) vs. distance from the Galactic center,  $R$ , analyzed over  $6.2 \leq |\ell| \leq 80^\circ$  for a flat rotation curve with  $V_\theta = 220 \text{ km s}^{-1}$ . The vertical line at  $R = 2.6 \text{ kpc}$  marks the approximate edge of the extended H I layer, which is found to smaller values of  $R$  than the H II regions.

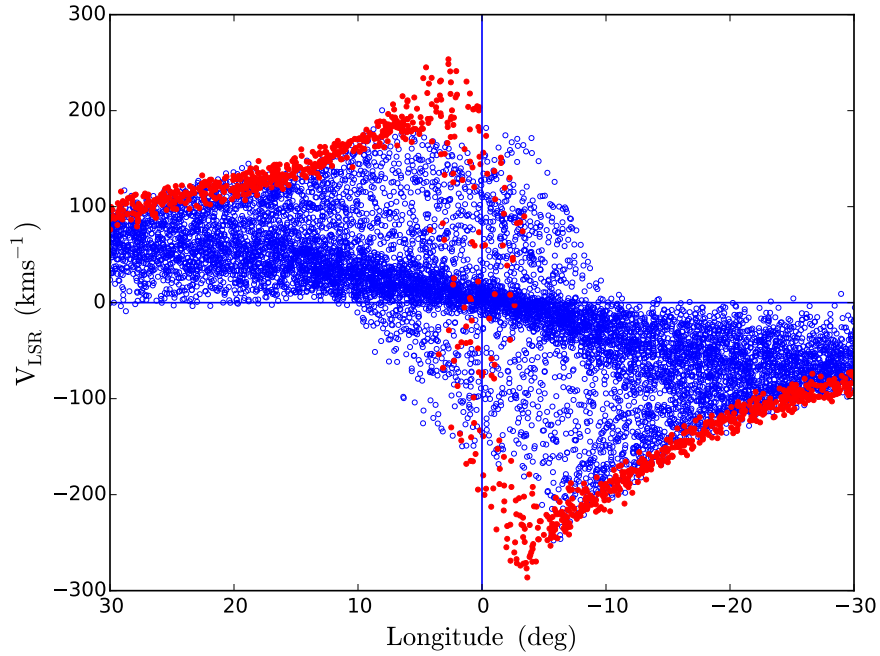


Fig. 6.— Velocity-longitude distribution of particles in a simulation using the WS kinematical bar model. Clouds within  $\pm 0.6$  kpc of the tangent point are marked in red. Except quite near the Galactic center, the tangent-point clouds cluster around the maximum velocity in their direction. Selection of H I at the maximum velocity, therefore, gives a sample of gas near the tangent points. To reduce confusion in this Figure near  $V_{\text{LSR}} \approx 0$ , only a random subset of the particles at  $R > 5$  kpc are plotted.

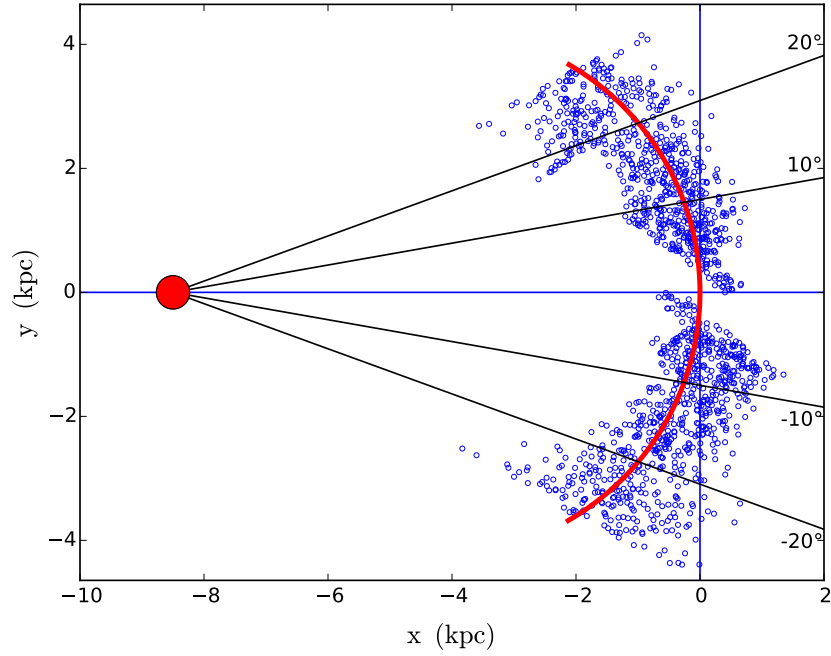


Fig. 7.— Location of simulated H I clouds selected according to the same criteria as were used in analysis of the the actual H I data. This gives an estimate of the area of the Galaxy sampled to produce Fig. 2 and Fig. 3. The location of the Sun is marked with a red circle and lines are drawn at various longitudes. The structure between longitudes  $10^\circ$  and  $20^\circ$  results from streaming along the model bar, which moves particles to velocities much lower than  $V_t$ . A similar effect does not occur in the South.